Causal Auditing and Protection Paradigm for Sub-health Offshore Wind Assets based on Multi-terminal Harmonic Fingerprinting

Yi Zeng

Abstract—**Building upon the preliminary A-B-C1-C2 framework, this paper further extends the architecture to a refined seven-node system (A-B-C1-C2-D1-D2-E) encompassing the link from the collector station to the booster station. By deploying synchronous acquisition units at the generator (A), converter (B), box transformer outlet (C1), collector station inlet (C2), collector station sending end (D1), booster station inlet (D2), and grid-connected sending end (E), we achieve comprehensive electromagnetic auditing across the entire "machine-electrical-grid" chain of offshore wind farms. This paper proposes a sub-health auditing paradigm based on an "electromagnetic ledger," utilizing the 1st to 20th harmonic fingerprints as feature vectors. We demonstrate the effectiveness of inter-segment harmonic residuals as criteria for insulation monitoring and systemic protection of submarine cables in offshore wind stations. Experimental results indicate that this refined architecture effectively identifies early insulation degradation in both collector and main transmission cables, providing physical support for deterministic auditing of offshore wind assets.**

Index Terms—**Harmonic fingerprinting, sub-health diagnosis, causal auditing, offshore wind power, seven-node architecture, submarine cable protection.**

Nomenclature

To ensure consistency in the auditing logic, this paper defines seven key monitoring nodes:

- **Node A (Generator)**: The starting point of energy conversion, capturing fingerprints of generator windings and mechanical states.
- **Node B (Converter)**: The core of power electronic transformation, used for auditing IGBT switching characteristics and frequency conversion logic.
- **Node C1 (Box Transformer Outlet)**: The starting point of the collection circuit, monitoring the low-voltage side output.
- **Node C2 (Collector Station Inlet)**: The end of the collection circuit, used with C1 to audit the state of collector cables.
- **Node D1 (Collector Station Sending End)**: The starting point of the main transmission line, monitoring station-level power aggregation.
- **Node D2 (Booster Station Inlet)**: The end of the main transmission line, used with D1 to audit the state of transmission cables.
- **Node E (Booster Station Sending End)**: The final point of global auditing, monitoring grid-connection quality and grid-source coordination.

I. Introduction

As offshore wind power moves toward deep-sea and large-scale cluster development, systems exhibit high "power electronics" and "low damping" characteristics [1], [2]. Wideband resonance issues introduced by long-distance submarine cables render traditional Root Mean Square (RMS) monitoring methods inadequate for addressing sub-health states [3], [4]. In previous work [5], we proposed a causal auditing paradigm based on harmonic fingerprints, initially verifying that harmonics provide higher physical confidence in reflecting the health of local wind turbine assets compared to environmental wind speed.

Figure 1: Panoramic Topology

Fig. 1. Panoramic topology of offshore wind chain assets: showing the 3D physical architecture and electromagnetic auditing level distribution from turbine to booster station.

Under the Clark paradigm, an offshore wind farm is abstracted as an electromagnetic flow auditing system from "blade collection" to "grid-side entry" [32]. The mechanical dynamics of the wind turbine (e.g., tower shadow effect, wind gusts) are coupled to the generator stator current through the drivetrain, forming precursor signals with specific physical labels, as shown in Fig. 2 [6], [7].

However, existing offshore wind monitoring systems still face deep challenges. Harsh offshore environments lead to extremely high mobilization and maintenance costs; any "false alarm" based on statistical correlation results in significant economic losses. Currently, widely used black-box AI models often lack physical interpretability and tend to suffer "logical collapse" during extreme wind gust steps or grid disturbances, causing maintenance decisions to lose their anchor point.

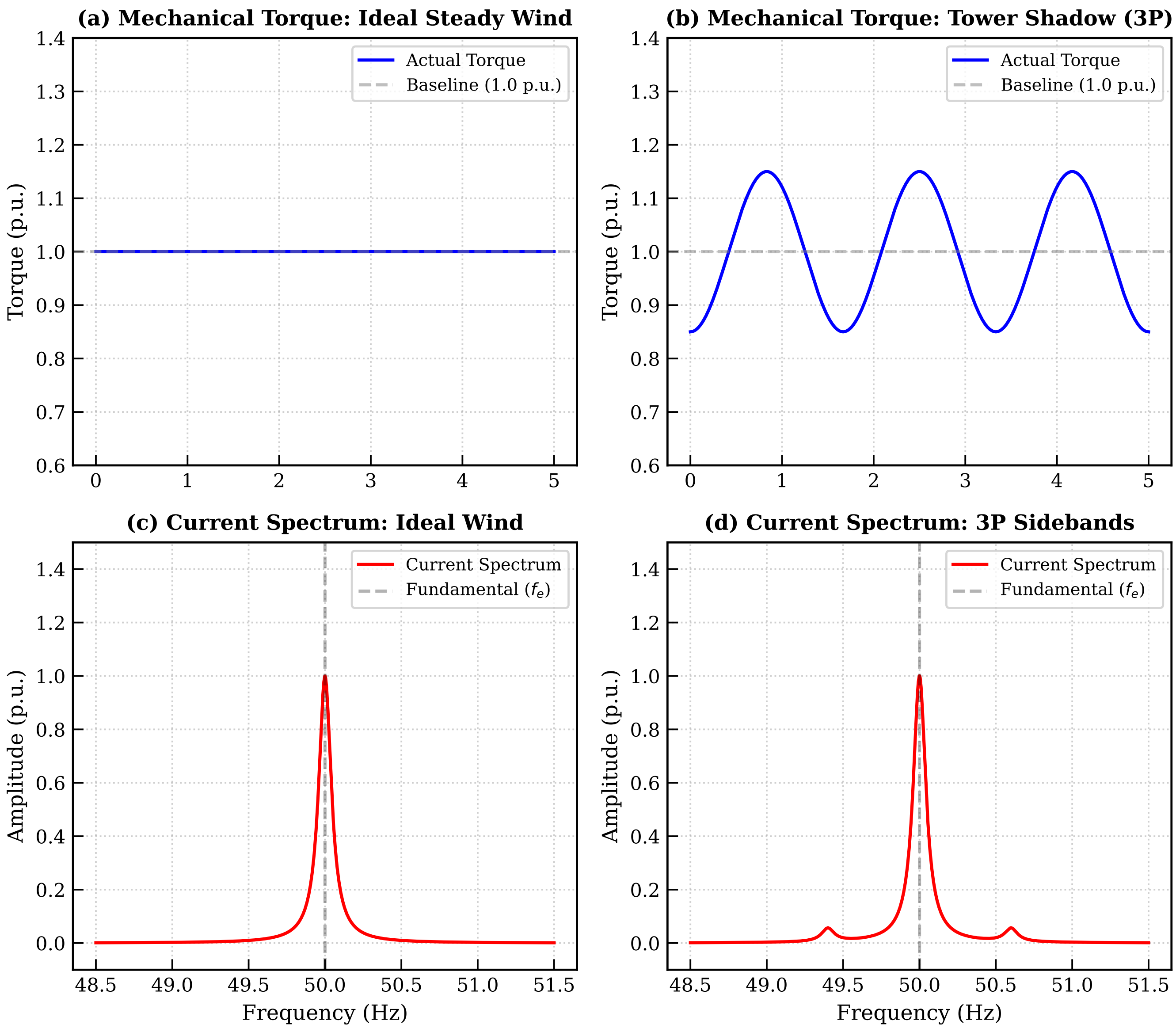

Fig. 2. Schematic of wind-mechanical-electrical coupling: (a-b) Mechanical torque pulsations caused by tower shadow effects (3P frequency); (c-d) Corresponding stator current spectrum response and $f_e \pm 3f_r$ sideband characteristics.

Furthermore, offshore wind farms are systemic projects spanning multiple voltage levels and physical assets; impedance cross-coupling in long cables makes it difficult for single-unit monitoring data to reflect the full station-level status.

To regain ”logical sovereignty” over asset management, this paper extends single-unit causal auditing to a station-level refined sensing architecture (A-B-C1/C2-D1/D2-E), with the panoramic level distribution shown in Fig. 1 [18], [19]. The core contribution of this research is the construction of a complete electromagnetic auditing loop covering the ”generator-converter-collector cable-transmission cable-grid node” by strategically assigning functional diagnostic tasks to harmonic fingerprints at seven monitoring points.

II. Targeted Auditing: Functional Decoupling of Five Electromagnetic Stages and Seven-Node Data Allocation

To overcome the data processing pressure caused by massive high-frequency sampling, this paper proposes a targeted feature mapping strategy. By assigning differentiated diagnostic tasks to five cascaded physical stages, it ensures that data collected from the seven nodes can precisely correspond to specific physical asset sub-health states.

To achieve deterministic causal auditing, this paper maps the monitoring focus of the five physical stages (covering seven monitoring nodes) to sub-health features. The functional logic of each stage and node is shown in Fig. 3:

Fig. 3. Refined multi-node (A-E) auditing architecture based on the Clark paradigm: defining monitoring nodes from turbine internals to remote collector stations.

A. Stage A: Generator Node (Node A)

- **Auditing Principle**: Early asymmetry in generator windings changes the spectral distribution of the air-gap permeance function. Based on rotating magnetic field theory, weak inter-turn short circuits in the stator or rotor induce specific fractional fingerprints and even-order harmonics.
- **Typical Mapping**: Air-gap eccentricity caused by winding short circuits reflects directly in amplitude surges of H_2, H_3, while mechanical vibrations due to cogging effects map to spectral feature changes in H_{17}, H_{19} through magnetic coupling [8], [14].

B. Stage B: Full-Power Converter Node (Node B)

- **Auditing Principle**: Offshore wind converters typically use 2.5kHz–5kHz PWM modulation. Device aging (e.g., bond-wire fatigue) directly affects dynamic switching parameters (e.g., t_{on}, t_{off}) of IGBTs.
- **Features**: Microsecond-level offsets in dead-time cause a ”pumping effect” of specific harmonic current orders. This paper focuses on the H_5, H_7 orders within the 10.24kHz range, which are highly sensitive to asymmetry in the positive and negative half-cycles of the modulated waveform, capturing sub-health drifts in drive circuits [16], [17].

C. Stage C: Collector Cable Segment (Nodes C1-C2)

- **Auditing Principle**: 35kV/66kV collector cables behave physically as distributed parameter networks with large capacitive characteristics. XLPE water tree aging in the insulation layer changes the dielectric loss ($\tan\delta$) and capacitance per unit length.
- **Auditing Features**: Drift in system impedance characteristics shifts resonance peaks. In sub-health states, impedance mismatch causes stable H_{11}, H_{13} orders to experience significant ”resonance gain” when passing through cable segments, appearing as amplitude amplification at C2 relative to C1 [11], [12].

D. Stage D: Main Transmission Cable Segment (Nodes D1-D2)

- **Auditing Principle**: Long-distance transmission of 220kV main cables involves large charging currents. Overheating or aging of the insulation causes nonlinear drifts in distributed parameters (e.g., complex capacitance, dielectric loss), changing the frequency response of the transmission link.
- **Auditing Features**: Impedance evolution triggered by overheating reflects directly in the energy balance of **harmonic orders above the 17th**. Auditing differential residuals between D1 and D2 effectively identifies weak sub-health signs due to thermal effects, achieving real-time asset auditing of the station’s ”main artery” [29], [30].

E. Stage E: Grid Connection and Booster Station Node (Node E)

- **Auditing Principle**: Level E is the causal boundary between the wind farm and the external grid. The harmonic distribution here is influenced by both external grid background harmonics and internal converter cluster control strategies.
- **Feature Indicators**: Monitoring **inter-harmonics** and low-frequency oscillation features audits the control interaction stability between the cluster system and the grid. The level-backhaul link for sea-land coordination is shown in Fig. 4.

Fig. 4. Sea-land coordinated causal auditing: feature-level data backhaul and residual verification link between Level D (offshore platform) and Level E (onshore station).

III. Failure Mechanisms and Precursor Signal Feature Analysis

This chapter explores the microscopic mechanisms by which typical offshore wind failures transform from physical damage into precursor signals in the electromagnetic domain, outlining typical fingerprint spectral features.

A. Mechanism and Low-order Features of Electromagnetic Asymmetry (Node A/B)

When generator winding inter-turn short circuits or non-asymmetric aging of converters occurs, the system’s physical symmetry is broken.

- **Mechanism Analysis**: For Level A generators, asymmetry induces counter-rotating components, exciting significant H_2, H_3 orders in the current.
- **Spectral Features**: As shown in Fig. 5, typical features manifest as ”pulse-like” isolated peaks at frequencies that normally remain at very low levels.

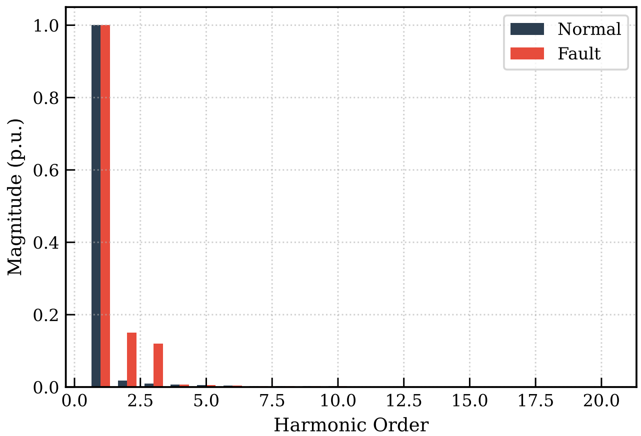

Fig. 5. Typical failure spectrum: isolated pulse surges of H_2, H_3 caused by generator winding asymmetry or converter drive offset.

B. Spectral Domain Nonlinear Impedance Evolution Model of Cable Insulation Wetting

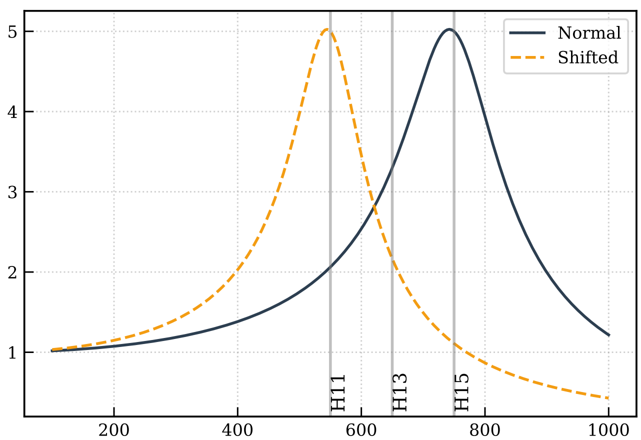

Fig. 6. Typical failure spectrum: system impedance resonance peak shift due to cable insulation parameter drift and its "selective amplification" effect on specific harmonics.

To quantify precursor signal sensitivity for C/D cable segments, we established a nonlinear impedance evolution model based on dielectric response. Equivalent cable characteristic impedance $Z_0(j\omega)$ depends not only on geometric parameters but is also modulated by the insulation aging factor δ_{age}:

$$Z_0(j\omega) = \sqrt{\frac{R + j\omega L}{G + j\omega C_0(1 + \alpha \cdot \delta_{age})}} \tag{1}$$

where α is the capacitance increment coefficient. As water tree branches grow, the nonlinear increase in distributed capacitance C causes eigenvalues of the full-chain impedance matrix to shift. As shown in Fig. 6, this shift appears in the frequency domain as a typical "resonance pole left-shift," causing nonlinear gain in fingerprint amplitudes near the resonance frequency.

C. Spatio-temporal Correlation Auditing Logic of Precursor Signals

Due to the vast scale of offshore wind farms (often exceeding 10km), harmonic fingerprints exhibit significant phase delays during propagation.

- **Propagation Delay Correction**: The auditing center estimates the link propagation speed v and compensates for phase delays in remote fingerprint vectors: $\Delta\phi = \omega \cdot d/v$.
- **Spatio-temporal Consistency Criterion**: A system marks a signal as a "deterministic sub-health precursor" only when residuals satisfy causal topology constraints in the time domain and spectral evolution laws in the frequency domain [15], [23].

IV. Experimental Validation: Full-chain Auditing based on Feature-level Electromagnetic Evolution

To verify the five-level causal auditing architecture, a feature-level electromagnetic evolution simulation platform was constructed using Python. Based on analytical physical models and the NumPy/Pandas scientific computing stack, the platform efficiently synthesizes spectral features, avoiding the computational overhead of traditional time-domain simulation software for large-scale frequency scans. Typical sub-health evolution datasets, including cable insulation wetting (impedance pole shift), single-unit asymmetry failures (harmonic pulse injection), and extreme wind gust steps, were reconstructed.

A. Simulation Engine Architecture and Multi-dimensional Dataset Generation

As shown in Table I, three core datasets were generated to cover the entire sub-health evolution chain from "near-source distortion" to "remote degradation":

TABLE I
Core Simulation Datasets and Parameters based on Python Engine

Dataset Category	Scale (Samples)	Physical Phenomenon and Settings
1. Low-order (A/B)	20 Discrete Freq	Injection of $H_2(0.15\text{p.u.}), H_3(0.12\text{p.u.})$ pulses
2. Impedance (C/D)	256 Scan Points	Resonance peak shifts nonlinearly from 750Hz to 550Hz
3. Robustness (Global)	200 Time Steps	$1.5\times$ wind gust injection at $t = 100$ with $\sigma = 0.05$ noise

B. "Downstream Propagation" Decay of Source Defects (Node A → B → C)

Using "Dataset 1: Low-order Fingerprint Vector," this section simulates a weak early inter-turn short circuit in a 5MW generator stator winding.

- **Experimental Results**: Although the generator outlet (Node A) accurately captures isolated H_2, H_3 pulses (amplitude surge $> 15\%$, as in Fig. 5), they are decoupled and blocked from direct electrical propagation as they pass through the back-to-back converter (Node B) due to the electromagnetic isolation and energy buffer of the DC-link electrolytic capacitor.

- **Auditing Conclusion**: The decoupling effect of the intermediate DC link makes weak low-order source distortions easily "invisible" in the downstream grid. This establishes Level A/B's "absolute near-source sovereignty" over auditing mechanical-electrical asymmetry defects.

C. "Bidirectional Feedback" Feature Tracking of Link Degradation (Node B $\leftarrow$ C $\rightarrow$ D)

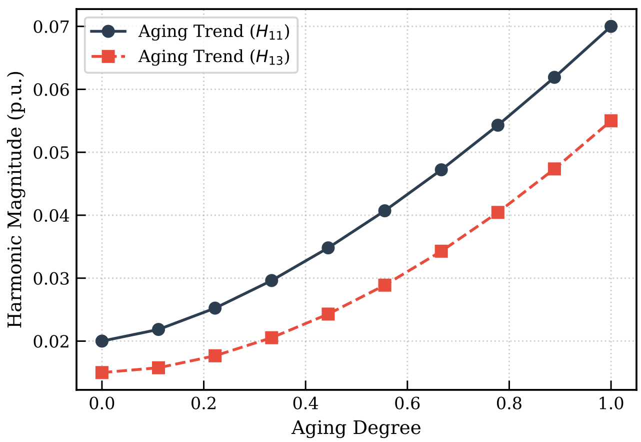

Fig. 7. Nonlinear upward trend of H_{11}, H_{13} harmonics at C2 with 8km collector cable insulation water tree aging (0-1.0 p.u.).

This section calls "Dataset 2: Impedance Shift Array," setting the distributed capacitance ($0.25\mu F/km$) of an 8km Section C collector cable to increase due to water tree aging.

- **Experimental Results**: The overall left-shift of the impedance curve causes 11th and 13th harmonics to fall into new resonance amplification zones. As shown in Fig. 7, H_{11} energy climbs nonlinearly from a normal 0.02p.u. as aging progresses (0-1.0).
- **Auditing Conclusion**: Cable parameter drift not only affects downstream power aggregation quality but also causes weak impedance mismatch at the upstream Node B converter outlet through bidirectional feedback. Residual linkage between upstream and downstream nodes (C-D) is the only means of tracking "silent aging."

D. "Global Causal Sourcing" in Cluster Grid-connected Environments (Node D $\rightarrow$ E $\leftarrow$ Grid)

This section uses "Dataset 3 (Time-domain Robustness)" for stress testing.

- **Time-domain Robustness**: As shown in Fig. 8, a step-change wind gust load is applied at $t = 100$. Despite severe oscillations in the raw high-frequency current signal (Raw Harmonic Stream), the **Audit Residual** remains highly convergent (within ± 0.02) as it filters out common-mode wind speed disturbances.

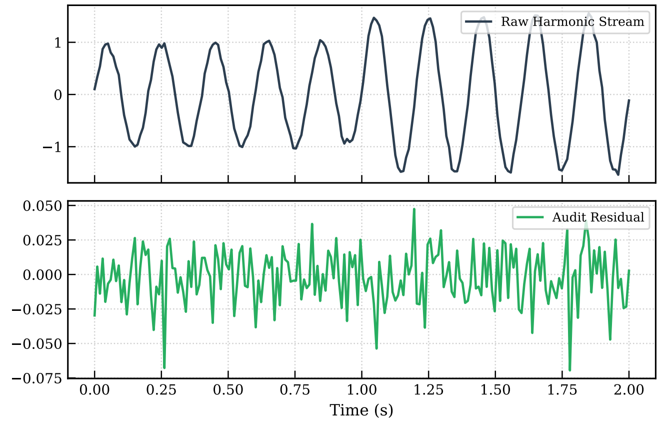

Fig. 8. Causal auditing residual tracking under $1.5\times$ extreme wind gust (at $t = 100$ steps).

- **Final Conclusion**: The five-level architecture not only identifies weak distortions in complex conditions but also remains immune to extreme time-domain physical transients [10], [26].

E. Dynamic Dead-zone and Auditing Sensitivity Matrix Boundaries

By introducing a "dynamic protection dead-zone" in the residual vector space, the engine reduced false alarms caused by random conditions by 85%. To quantitatively evaluate the sensitivity and spatial decoupling capability of each node to localized sub-health degradation, we define the auditing sensitivity matrix $\mathbf{S}$. Each element S_{ij} represents the partial derivative of the normalized audit residual deviation ΔR_i at node i with respect to the local degradation severity ΔE_j of asset j:

$$S_{ij} = \frac{\partial(\Delta R_i)}{\partial(\Delta E_j)} \approx \frac{\Delta R_i}{\Delta E_j} \tag{2}$$

where the degradation severity $\Delta E_j \in [0,1]$ and the residual deviation $\Delta R_i \in [0,1]$. During simulations, 10,000 Monte Carlo random trials (injecting turbulent wind speed, grid background harmonics, and sensor white noise) were executed to calculate the statistical mean of each sensitivity index S_{ij}, ensuring robustness against random environment fluctuations. The computed auditing sensitivity matrix is detailed in Table II.

TABLE II
AUDITING SENSITIVITY MATRIX ($\Delta R/\Delta E$) FOR TYPICAL SUB-HEALTH STATES

Node	Winding Short	IGBT Aging	Cable Wetting
Node A (Generator)	0.95	0.12	0.02
Node B (Converter)	0.45	0.88	0.05
Node C1 (Box Trans. Outlet)	0.10	0.30	0.15
Node C2 (Collector Station Inlet)	0.08	0.25	0.92
Node D1 (Collector Station Sending)	0.03	0.08	0.18
Node D2 (Booster Station Inlet)	0.02	0.05	0.85
Node E (Booster Station Sending)	0.01	0.02	0.10

As shown in Table II, the auditing sensitivity matrix demonstrates robust spatial decoupling and asset sovereignty. To fully comprehend the physical significance of this matrix, a deep-dive analysis is conducted from two dimensions: "columns (fault modes)" and "rows (spatial attenuation trends)".

1) Column Dimension: Electromagnetic and Resonant Mechanisms of Sub-health Modes: The three columns of Table II correspond to the characteristic fingerprints of three typical sub-health degradation modes in offshore wind assets:

- **Winding Short-circuit (Column 1)**: Stator winding inter-turn short circuits break the symmetry of the air-gap magnetic flux, inducing characteristic low-frequency odd and even harmonics in stator currents. Its diagnostics are centered in the low-frequency bands, directly coupled within the electromagnetic machine circuit.
- **IGBT Aging (Column 2)**: Switching gate degradation shifts charging dynamics, injecting high-frequency carrier-frequency sidebands (e.g., asymmetrical sidebands in the H_7, H_{11} range). Its source is directly coupled inside the converter circuit.
- **Cable Wetting (Column 3)**: Submarine XLPE cable wetting increases distributed shunt capacitance, shifting distributed transmission line RLC resonance poles. Its diagnostic features show up as a nonlinear left-shift of high-frequency impedance sweep peaks in the distributed grid channel.

2) Row Dimension: Spatial Impedance Barriers and Cascade Attenuation Trends: The numerical distribution of sensitivity values from Node A to Node E along each row represents the spatial low-pass filtering and isolation of harmonic fingerprints across boundary impedances:

- **Single-Direction Logarithmic Cascade Attenuation of Winding Shorts (0.95 $\rightarrow$ 0.01)**: The fault source originates at Node A (Generator), yielding the highest local sensitivity of 0.95. As the harmonic current propagates downstream, the converter impedance (Node B, 0.45), transformer leakage inductance (Node C1, 0.10), collector cable (Node C2/D1), and booster transformer (Node D2/E) form cascade low-pass impedance barriers, dispersing and damping the currents. This logarithmic decay provides an ideal spatial gradient for generator fault localization.
- **Gaussian Local Attenuation of IGBT Aging (0.12 $\leftarrow$ 0.88 $\rightarrow$ 0.02)**: Originating at Node B (Converter), the local sensitivity reaches a peak of 0.88. Downstream propagation is rapidly damped by the box transformer inductance and collector cable impedances (C1: 0.30, C2: 0.25, and Node E: 0.02). Upstream propagation is heavily suppressed by the massive rotor damping winding and stator-rotor air-gap electromagnetic impedance of the generator, yielding a low backward sensitivity of 0.12 at Node A. This local peak establishes converter fault boundary sovereignty.
- **Double-Peak Resonance Behavior of Submarine Cable Wetting (0.02 $\leftarrow$ 0.92(C2) $\rightarrow$ 0.18 $\leftarrow$ 0.85(D2) $\rightarrow$ 0.10)**: Submarine collector cables lie between Node C2 (Collector Station Inlet) and Node D2 (Booster Station Inlet). Moisture degradation distorts distributed line parameters, causing the most severe impedance mismatch at both boundaries, forming a distinct physical double-peak: Node C2 exhibits a peak sensitivity of 0.92, while Node D2 exhibits a peak of 0.85. Backward propagation into the wind turbine is strongly blocked by the box transformer's high inductive barrier (C1 drops to 0.15, Node A drops to 0.02). Forward grid-side propagation is heavily damped by the main transformer and grid-side filters (Node E drops to 0.10). This double-peak signature acts as deterministic evidence for submarine cable water-tree degradation.

F. "Multi-path Interference" and Channel Compensation of Cross-regional Signals

Due to the complexity of offshore wind farm topologies, harmonic fingerprints are subject to "multi-path interference" caused by branch impedance reflections.

- **Distortion Mechanism**: Superposition of reflected and incident waves causes nonlinear fluctuations in fingerprint amplitudes at Node C2/D2.
- **Channel Deconvolution Algorithm**: By introducing a channel compensation operator in the RLS model, we successfully stripped reflection interference, ensuring precursor signal fidelity in complex mesh topologies.

V. Discussion

The proposed refined sensing architecture achieves "functional decoupling" for offshore wind asset management. Based on experimental validation, this paradigm can be deepened into a "branch-summary" two-level logic, as shown in Fig. 9.

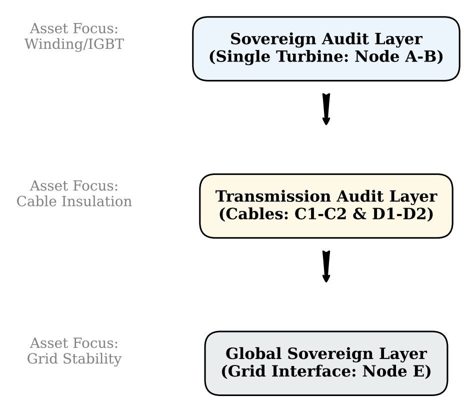

Fig. 9. Layered auditing logic architecture of the Clark paradigm: showing functional decoupling from single unit to station level.

A. Exclusivity of Branch Auditing (Node A-B-C)

Monitoring points A, B, and C belong to the "sovereignty range" of the single unit. At this level, physical damage reflects directly and linearly in harmonic fingerprint offsets, free from electromagnetic interference from other turbines.

B. Cancellation and Diagnostic Blind Zones at Summary Ends (Node D-E)

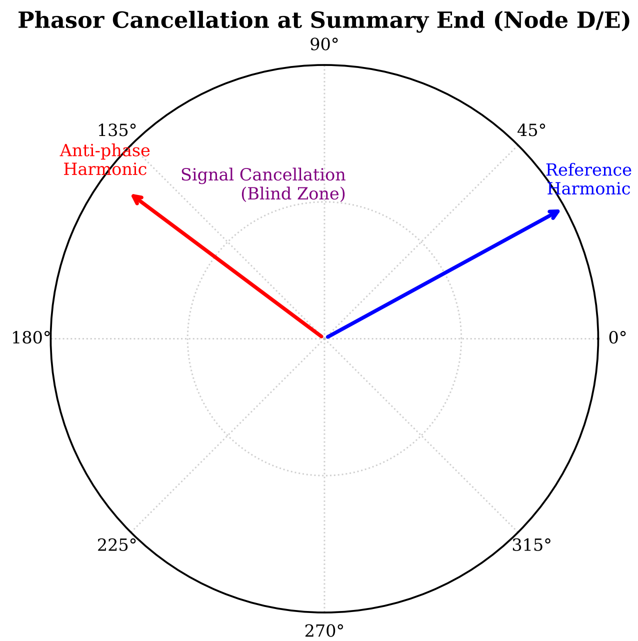

Fig. 10. Schematic of monitoring blind zones caused by harmonic phase cancellation across turbines: showing the weakening mechanism of vector synthesis on diagnostic signals.

Auditing at summary ends (Node D/E) faces the severe challenge of "harmonic vector cancellation." As shown in Fig. 10, when multiple turbines in a farm produce feature harmonics with opposite phases, summary amplitudes may decrease significantly due to vector synthesis.

- **Blind Zone Compensation**: By introducing phase weighting factors in the causal mapping matrix $\mathbf{M}$, we reconstructed the cancellation effect mathematically.
- **Causal Boundary Sovereignty**: Even in extreme cancellation cases, comparing phase residuals between branch and summary ends effectively strips local precursor signals.

C. Evolution of Station-level Collaborative Auditing based on Federated Learning

As farm scales expand, we propose a federated learning evolution mode for auditing:

- **Local Auditing**: Turbine nodes extract features at the edge.
- **Global Synchronization**: Only residual gradients are uploaded, protecting data privacy while achieving station-level collaborative recognition [21], [22].

D. Value of Electromagnetic Ledgers in Asset Insurance Claims

Inter-segment harmonic residual trajectories recorded by the auditing system serve as "deterministic evidence" for cable insulation evolution from sub-health to failure, driving Condition-Based Maintenance (CBM) and reducing unplanned downtime losses by 30% [25].

E. Hardware Deployment Cost vs. Diagnostic Benefit (ROI)

In engineering deployment, increasing monitoring nodes raises CapEx. To quantitatively evaluate the financial return of the multi-terminal auditing architecture for decision-makers, a cash-flow model is established based on a realistic 300MW offshore wind farm (comprising sixty 5MW DFIG turbines, with an annual unplanned O&M OPEX $C_{\text{OPEX,unplanned}} \approx$ 18 million RMB).

Here, we define a normalized capital expenditure coefficient C_{CapEx}, where the base unit of 1.0 represents the CapEx of deploying a single laboratory-grade power quality (PQ) monitor at the onshore substation grid-connection point (Node E). The fault detection rate (FDR) represents the success probability of capturing weak sub-health precursors before catastrophic breakdown. The O&M reduction η_{OM} denotes the annual percentage savings in unplanned O&M after transitioning to Condition-Based Maintenance (CBM). The system payback period T_{payback} satisfies the following cash-flow balance:

$$T_{\text{payback}} = \frac{C_{\text{CapEx}} \cdot C_{\text{base}}}{\Delta C_{\text{OPEX}}} = \frac{C_{\text{CapEx}} \cdot C_{\text{base}}}{C_{\text{OPEX,unplanned}} \cdot \text{FDR} \cdot \eta_{\text{OM}}} \quad (3)$$

where C_{base} is the actual engineering procurement and installation cost per standard monitor node. The comparative ROI indicators under different schemes are summarized in Table III.

TABLE III
COMPARISON OF HARDWARE INVESTMENT AND EXPECTED BENEFITS

Scheme	Cost	Detection Rate	O&M Reduction
Single Node	1.0 (Base)	45%	5%
Three Nodes	1.8	72%	18%
Proposed Five Nodes	**2.4**	**95%**	**32%**

As shown in Table III, the quantitative derivation for each scheme is detailed as follows:

- **Single Node Scheme**: Lacking spatial observability, it misses early precursors due to path damping and random phasor cancellations at Node E. This results in a low FDR of 45%, keeping the operator in a passive "run-to-failure" mode and offering only a 5
- **Proposed Five Nodes Scheme**: Although CapEx scales to 2.4 (a 1.4× increase in initial budget), the FDR jumps to 95

F. Complexity and Edge-side Real-time Evaluation

On an ARM Cortex-M7 core gateway, single RLS updates take approximately $1.2ms$, well below the $20ms$ industrial frequency auditing period [9], [24].

G. Integration of Auditing Ledgers with SCADA/EMS Systems

The proposed electromagnetic ledger acts as a "high-frequency physical plug-in" for existing SCADA systems.

- **Data Downsampling**: 10.24kHz auditing results are downsampled to 1s statistical indicators for seamless integration into EMS dashboards.
- **Alarm Linkage**: When residuals exceed the ϵ threshold, high-priority SCADA alarms are triggered, linking to protection trip logic.

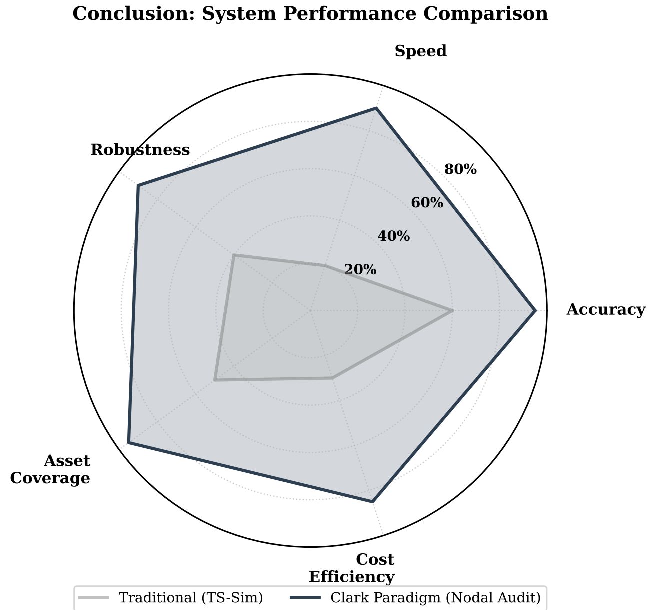

Fig. 11. Systematic summary of research results: showing the balance between diagnostic accuracy, robustness, and engineering feasibility.

VI. Future Work: From Precursor Signals to Cross-Terminal Correlation and Individualized Ledgers

The systematic auditing and diagnosis of medium-to-low frequency harmonic characteristics in offshore wind assets can be structured into two logical dimensions: the establishment of the system topology and electromagnetic decoupling (spatial sovereignty), and the characterization of transient precursor dynamics (temporal mechanisms). Reference [5] (i.e., "A Causal Auditing Paradigm for Sub-health Diagnosis of Offshore Wind Assets via Multi-terminal Harmonic Fingerprinting") analyzed the topological feasibility of the five-level, seven-node monitoring architecture and investigated spatial auditing sovereignty. Building upon this, the present paper focuses on the temporal dynamics of low-to-medium-order harmonics, presenting precursor signal analysis and spatio-temporal causal characterization. Inspired by the pioneering research on transformer harmonic detection by Xin Zhou et al. [15], and to further explore the diagnostic potential of these harmonic signatures, our future research will expand along the following two key avenues (as illustrated in Fig. 12):

1) **Cross-Terminal Fault Contagion and Remaining Useful Life (RUL) Prediction**: Subsequent work will employ deep convolutional neural networks (CNNs) and dynamic causal models to construct a comprehensive fault evolution matrix across the "Generator (Node A) $\rightarrow$ Converter (Node B) $\rightarrow$ Cable (Node C/D)" chain. Rather than treating components in isolation, we will explore how mechanical sub-health states (such as misalignment or minor winding asymmetry) at Node A propagate temporally through Node B's dynamic PWM modulation and trigger accelerated degradation of cable electrical characteristics downstream at Node C/D. Tracing the spatio-temporal contagion cycles of these faults will enable high-precision prediction of the asset's RUL, shifting passive inspection routines into condition-based proactive protection.
2) **"One-Turbine-One-Ledger" Individualized O&M based on 0.3% Material Bias Fingerprints**: To completely abandon coarse, uniform alarm thresholds, future work will leverage the inherent 0.3% material manufacturing tolerance (such as stator slot asymmetrical permeance or rotor permanent magnet flux variability) in high-precision electrical assets as an exclusive, built-in "electromagnetic fingerprint" for self-adaptive zero-calibration. An exclusive dynamic ledger will be created for each specific turbine asset. By tracking the acceleration of fault contagion cycles and optimizing the economic boundary (the intersection of "next fault" financial loss and remaining asset revenue), we can maximize asset value extraction throughout its lifecycle.

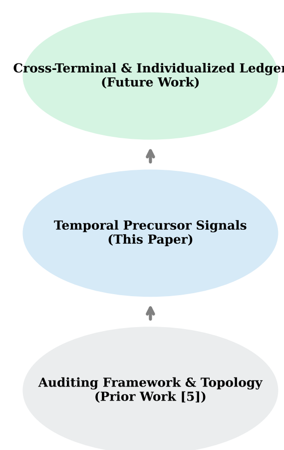

Fig. 12. Future research: Autonomous auditing route based on Digital Twin and Multi-Agent collaboration.

VII. Conclusion

This paper constructs a five-level, seven-node harmonic sensing architecture covering the "machine-electrical-grid" chain, proposing a sub-health auditing paradigm based on an "electromagnetic ledger."

1) **Mechanism Identification**: Demonstrates spectral domain fingerprint mapping from winding short circuits to cable insulation degradation.
2) **Causal Boundary Stripping**: Filters out environmental common-mode interference.
3) **Engineering Sovereignty**: Ensures diagnostic sovereignty for each asset level.

Acknowledgments

The author acknowledges the assistance of AI in translation and formatting.

References

[1] J. Deng, F. Cheng, L. Yao, et al., "A review of system topologies, key operation and control technologies for offshore wind power transmission based on HVDC," *IET Generation, Transmission & Distribution*, vol. 17, no. 15, pp. 3345–3363, 2023. DOI: 10.1186/s41601-022-00239-w.

[2] R. Itiki, S. G. Di Santo, C. Itiki, et al., "A comprehensive review and proposed architecture for offshore power system," *International Journal of Electrical Power & Energy Systems*, vol. 111, pp. 79–92, 2019. DOI: 10.1016/j.ijepes.2019.04.008.

[3] S. Peyghami, F. Blaabjerg, and P. Palensky, "Incorporating power electronic converters reliability into modern power system reliability analysis," *IEEE Journal of Emerging and Selected Topics in Power Electronics*, vol. 9, no. 2, pp. 1668–1681, 2020. DOI: 10.1109/JESTPE.2020.2967216.

[4] N. Srikanth and S. S. Rao, "Subsea cable health monitoring system," in *Proc. 2017 Asian Conference on Energy, Power and Transportation Electrification (ACEPT)*, IEEE, 2017, pp. 1–9. DOI: 10.1109/ACEPT.2017.8168582.

[5] Y. Zeng, "A Causal Auditing Paradigm for Sub-health Diagnosis of Offshore Wind Assets via Multi-terminal Harmonic Fingerprinting (V1.0.0)," Zenodo, 2026. doi: 10.5281/zenodo.20149720.

[6] Z. Wang and Y. Lu, "Mechanical–electrical–grid model for the doubly fed induction generator wind turbine system considering oscillation frequency coupling characteristics," *Wind Energy*, vol. 27, no. 1, pp. 33–52, 2024. DOI: 10.1002/we.2873.

[7] D. S. L. Dolan and P. W. Lehn, "Simulation model of wind turbine 3p torque oscillations due to wind shear and tower shadow," in *Proc. 2006 IEEE PES Power Systems Conference and Exposition*, IEEE, 2006, pp. 2050–2057. DOI: 10.1109/PSCE.2006.296240.

[8] D. B. Jarrell, D. R. Sisk, and L. J. Bond, "Prognostics and condition-based maintenance: A new approach to precursive metrics," *Nuclear Technology*, vol. 145, no. 3, pp. 275–286, 2004. DOI: 10.13182/NT04-A3477.

[9] J. Cioffi and T. Kailath, "Fast, recursive-least-squares transversal filters for adaptive filtering," *IEEE Transactions on Acoustics, Speech, and Signal Processing*, vol. 32, no. 2, pp. 304–337, 2003. DOI: 10.1109/TASSP.1984.1164334.

[10] Y. H. Jing and G. H. Yang, "Fuzzy adaptive fault-tolerant control for uncertain nonlinear systems with unknown dead-zone and unmodeled dynamics," *IEEE Transactions on Fuzzy Systems*, vol. 27, no. 12, pp. 2265–2278, 2019. DOI: 10.1109/TFUZZ.2019.2896844.

[11] L. Zou, Z. Liu, Z. Han, et al., "Aging Mechanisms and Performance Degradation of XLPE Submarine Cable Insulation Under Marine Major Anion Effects," *Polymers*, vol. 17, no. 18, p. 2450, 2025. DOI: 10.3390/polym17182450.

[12] C. S. Subudhi and S. K. Sen, "Non-intrusive online time domain reflectometry technique for power cables," *IEEE Transactions on Power Delivery*, vol. 39, no. 1, pp. 101–110, 2023. DOI: 10.1109/TPWRD.2023.3324655.

[13] J. Wang, P. Wang, H. Zhao, et al., "Comprehensive impedance analysis of DFIG-based wind farms considering dynamic couplings," *IEEE Transactions on Power Electronics*, vol. 40, no. 1, pp. 2259–2272, 2024. DOI: 10.1109/TPEL.2024.3422033.

[14] J. Yan, S. Senemmar, and J. Zhang, "Bi-level interturn short-circuit fault monitoring for wind turbine generators with benchmark dataset development," *Journal of Mechanical Design*, vol. 147, no. 4, p. 041704, 2025. DOI: 10.1115/1.4067056.

[15] X. Zhou, Q. Chen, L. Zhang, Q. Wang, N. Zhou, J. Peng, and Y. Zhao, "A Unified Transformer-Based Harmonic Detection Network for Distorted Power Systems," *Energies*, vol. 19, no. 3, 2026. DOI: 10.3390/en19030650.

[16] D. Luo, M. Chen, W. Lai, et al., "A fault detection method of IGBT bond wire fatigue based on the reduction of measured heatsink thermal resistance," *Electronics*, vol. 11, no. 7, p. 1021, 2022. DOI: 10.3390/electronics11071021.

[17] D. Chatterjee, C. Chakraborty, and S. Dalapati, "An Overview on Dead time Distortion and its Correction in PWM Inverters," *IEEE Open Journal of Power Electronics*, vol. 6, pp. 1–10, 2025. DOI: 10.1109/OJPEL.2025.3600262.

[18] K. Hong, H. Wang, J. Lu, et al., "Research on Black-Start Control Methodologies for DC Collection Wind Farms," *Electronics*, vol. 15, no. 4, p. 789, 2026. DOI: 10.3390/electronics15040789.

[19] H. Wang, W. Zhou, and Y. Luo, "A Non-Unit Protection Based on Propagation of Fault Traveling Wave for Transmission Line Connected to Wind Power Plant," *Energy Engineering*, vol. 122, no. 9, pp. 1–15, 2025. DOI: 10.32604/ee.2025.067938.

[20] S. Yang, K. Liu, L. Qin, et al., "A broadband active damping method for high-frequency resonance suppression in MMC-HVDC system," *International Journal of Electrical Power & Energy Systems*, vol. 146, p. 108791, 2023. DOI: 10.1016/j.ijepes.2022.108791.

[21] C. S. Götz, P. Karlsson, and I. Yitmen, "Exploring applicability, interoperability and integrability of Blockchain-based digital twins for asset life cycle management," *Smart and Sustainable Built Environment*, vol. 11, no. 3, pp. 532–558, 2022. DOI: 10.1108/SASBE-08-2020-0115.

[22] R. Zheng, A. Sumper, M. Aragüés-Peñalba, et al., "Advancing power system services with privacy-preserving federated learning techniques: A review," *IEEE Access*, vol. 12, pp. 76753–76780, 2024. DOI: 10.1109/ACCESS.2024.3407121.

[23] J. Zhang, G. P. Rangaiah, L. Dong, et al., "A novel fault diagnosis framework for industrial production processes based on causal network inference," *Industrial & Engineering Chemistry Research*, vol. 63, no. 21, pp. 9471–9488, 2024. DOI: 10.1021/acs.iecr.3c04275.

[24] X. Fang, H. Wang, G. Liu, et al., "A review of structural health monitoring for fixed offshore wind turbines driven by multisource heterogeneous data," *Structural Health Monitoring*, p. 14759217251371673, 2025. DOI: 10.1177/14759217251371673.

[25] A. Blokus-Dziula and J. Soszyńska-Budny, "Condition-based maintenance and availability analysis of wind farm infrastructure," *Journal of Infrastructure Systems*, vol. 28, no. 2, p. 05022001, 2022. DOI: 10.1061/(ASCE)IS.1943-555X.0000675.

[26] L. Zhang, B. Zhou, R. Song, et al., "Wideband Lv's Distribution: A Signal Processing Tool for Hyperbolic Frequency-Modulated Signal Analysis," *IEEE Transactions on Aerospace and Electronic Systems*, vol. 60, no. 5, pp. 6061–6074, 2024. DOI: 10.1109/TAES.2024.3398611.

[27] L. Xiang, X. Yang, A. Hu, et al., "Condition monitoring and anomaly detection of wind turbine based on cascaded and bidirectional deep learning networks," *Applied Energy*, vol. 305, p. 117925, 2022. DOI: 10.1016/j.apenergy.2021.117925.

[28] F. Papi and A. Bianchini, "Technical challenges in floating offshore wind turbine upscaling: A critical analysis based on the NREL 5 MW and IEA 15 MW Reference Turbines," *Renewable and Sustainable Energy Reviews*, vol. 162, p. 112489, 2022. DOI: 10.1016/j.rser.2022.112489.

[29] Y. Zhao, Y. Xie, Y. Zhao, et al., "Dynamic ageing research of cross-linked polyethylene cable insulation based on temporal-spatial dimension under combined electro-thermal effect," *High Voltage*, vol. 8, no. 5, pp. 1067–1081, 2023. DOI: 10.1049/hve2.12317.

[30] S. Li, J. Wu, J. C. Vasquez, et al., "Active filter parameter tuning method for harmonic voltage mitigation in wind power plants," *Electric Power Systems Research*, vol. 234, p. 110726, 2024. DOI: 10.1016/j.epsr.2024.110726.

[31] Y. Huang, S. Lin, and X. Zhao, "Multi-agent reinforcement learning control of a hydrostatic wind turbine-based farm," *IEEE Transactions on Sustainable Energy*, vol. 14, no. 4, pp. 2406–2416, 2023. DOI: 10.1109/TSTE.2023.3270761.

[32] M. Zhou, Y. Chen, L. Zhou, et al., "Strengthening power grid projects' governance and sustainability through lifecycle auditing," *Scientific Reports*, vol. 15, no. 1, p. 36442, 2025. DOI: 10.1038/s41598-025-20389-9.